Journal of Alloys and Compounds 886 (2021) 161206

Contents lists available at ScienceDirect

Journal of Alloys and Compounds

journal homepage: www.elsevier.com/locate/jalcom

Nanostructured Mn-doped CeO_2 thin films with enhanced electrochemical properties for pseudocapacitive applications

Iheke Micheal Nwachukwu[a], Assumpta Chinwe Nwanya[a,b,*], Rose Osuji[a,c,d], Fabian I. Ezema[a,c,d]

[a] Department of Physics and Astronomy, University of Nigeria, Nsukka, Nigeria
[b] SensorLab, (University of the Western Cape Sensor Laboratories), 4th Floor Chemical Sciences Building, Robert Sobukwe Road, Bellville 7535, Cape Town, South Africa
[c] UNESCO-UNISA Africa Chair in Nanosciences-Nanotechnology, College of Graduate Studies, University of South Africa, Muckleneuk Ridge, South Africa
[d] Nanosciences African Network (NANOAFNET), iThemba LABS-National Research Foundation, 1 Old Faure road, Somerset West 7129, PO Box 722, Somerset West, South Africa

ARTICLE INFO

Article history:
Received 17 June 2021
Received in revised form 14 July 2021
Accepted 15 July 2021
Available online 17 July 2021

Keywords:
Cerium oxide
Manganese
Pseudocapacitors
SILAR
Specific capacitance

ABSTRACT

Cerium oxides with variable oxidation states, high interfacial charge transfer rate have demonstrated to be a potential pseudocapacitive material. In this paper, we present the structural and electrochemical properties of undoped and Mn-doped CeO_2synthesized using successive ionic layer adsorption and reaction(SILAR) method. The structural results as obtained from x-ray diffraction (XRD) confirmed the cubic fluorite structure of CeO_2 which was unaltered despite the doping concentration. However, a tensile strain of ~2.3% was observed due to ionic radii difference. The topography showed a porous network of nanograins, accounting for strong redox interfacial charge transfer. A specific capacitance of 690 Fg^{-1} was obtained for 5 wt% Mn-doped CeO_2, from cyclic voltammetry curve at a scan rate of 10 mV/s. This value is considerably higher than what was obtained for the undoped ceria, indicating that doping with Mn improved the electrochemical performance of the ceria films.

1. Introduction

Reducing fossil fuel consumption and greenhouse emissions has become a global objective that is imperative for the world's sustainability. Recently, many researchers have given much attention to energy storage systems such as capacitors, supercapacitors, batteries and fuel cells since alternative renewable energy resources that are being advocated for are not always available. Hence, it is imperative to store energy from these renewable energy resources to be used when they are not available as well as for off grid applications. Among energy storage systems, electrochemical capacitors (ECs) otherwise called supercapacitors have received much interest as they are characterized by higher specific power of several orders of magnitude compared to most batteries and fuel cells [1,2]. Electrode materials for ECs include carbon-based materials (graphene, CNT etc), metal oxides (CeO_2, RuO_2, Fe_2O_3 etc.) and conducting polymers (polyaniline, polypyrrole, polythiophene etc.). Development of new electrochemical supercapacitor electrode material has been recently deployed to overcome the challenges of low energy density. This has been achieved by hybridizing the electrode materials through the addition of electrochemically active materials to a carbon-particle-based energy storage (ES) electrode layer or totally replacing the carbon materials with electrochemically active materials [2].

In the fabrication of supercapacitors and improvement of electrochemical performance of pseudocapacitors, materials with high porosity and large surface areas are highly suitable [3,4]. Despite the intrinsic properties of ruthenium and iridium oxides, its applications are greatly affected by high cost, scarcity and high toxicity [5,6]. Due to these inadequacies, exploration of electrode materials such as CeO_2, MnO_2, NiO, Co_3O_4, Fe_2O_3 amongst others have gained much attention by researchers [7–9]. However, CeO_2 has been proven convenient, conducive and promising electrode material for supercapacitors due to its low toxicity, abundance and outstanding redox properties. Because of its redox property, it is used as a promising and convenient electrode material for supercapacitors [10].

Various CeO_2 composites, such as graphene-CeO_2 [11,12], GO-CeO_2 [13], SnO_2-CeO_2 [14], CNTs@CeO_2 hollow nanotubes [15] and rGO-CeO_2 [16], with specific capacitances that is higher than that of the undoped

* Corresponding author at: Department of Physics and Astronomy, University of Nigeria, Nsukka, Nigeria
E-mail address: chinwe.nwanya@unn.edu.ng (A.C. Nwanya).

https://doi.org/10.1016/j.jallcom.2021.161206
0925-8388/

CeO_2 have been successfully synthesized and reported. Hua et al. [17], synthesized ceria/ZnO composite using ultrasonic assisted successive ionic layer adsorption and reaction (SILAR) method and the films were used in catalysis. Moreover, a specific capacitance of 1027.8 Fg^{-1} has been reported by Cui et al. using hydrothermal approach to synthesize multilayered CeO_2 such as $NiO/MnO_2/CeO_2$ hybrid nanoflake arrays [18]. However, this synthesis involves a laborious process with several calcination steps and the hydrothermal method is prone to wide dimension standard deviation making it difficult to precisely control the final size and morphology of the films. Although most papers reported composites and multilayered materials, a recent work showed that only the nanostructured CeO_2 presents high capacitance of 927 Fg^{-1} at 2 Ag^{-1} current density [19]. Doping of CeO_2 is also a promising strategy to improve the electrochemical performance of this material since the specific capacitance enhancement and cyclic stability of CeO_2 nanostructures is based on the availability of valence 4f electrons [20]. In this way, some works have been carried out by doping the CeO_2 with Mn [21], noble metals like Ag and transition metals like La, Mn, Co or Ni [20] and Fe [22]. It was demonstrated that specific capacitance and electrochemical stability were enhanced with transition metal doping in particular with Mn dopant [14]. However more work is needed to optimize the dopant percentage and understand the physical processes involved as well as the development of simple, low-coast and highly reproducible synthesis methods. Therefore, an easily achievable synthesis approach that supports large surface area fabrication on different types substrates is successive ionic layer adsorption and reaction (SILAR) method which operates with the principle of the immersion of substrates into separately placed cationic and anionic precursors. SILAR method is one of the modified chemical methods for depositing uniform and large area thin films. In addition, precipitate formation in the solution is minimized. Furthermore, the deposition rate and the thickness of the films can easily be controlled over a given range of cycles and local over heating which may be detrimental to the deposited films can be avoided. Few reports have been published on the synthesis of CeO_2 using SILAR method [17]. However, to the best of the knowledge of the authors, no report of Mn-doped CeO_2 synthesized using the SILAR method and tailored to energy storage application has been reported. Therefore, this work is among the first attempt towards the use of Mn doped cerium oxide synthesized via SILAR method for pseudocapacitor application.

2. Materials and methods

We used analytical grade of chemicals which include cerium nitrate hexahydrate ($Ce(NO_3)_3.6H_2O$), manganese acetate ($CH_3.(COO)_2Mn\ 0.4H_2O$) and hydrogen peroxide (H_2O_2) and all were obtained from Sigma-Aldrich company. They were used without further purification.

2.1. Preparation of undoped CeO_2 and Mn-doped CeO_2 thin films

The immersion of substrates into separately placed anion and cation precursor solutions employed in this experiment obeys the principle of successive ionic layer adsorption and reaction technique. As illustrated in Fig. 1, four beakers were used for the deposition of undoped and Mn-doped CeO_2 thin films on substrates. Substrate pretreatment procedures have been described elsewhere [23].

Mn-doped CeO_2 thin films were prepared using ($Ce(NO_3)_3.6H_2O$) and $CH_3.(COO)_2Mn\ 0.4H_2O$ (for various concentration of Mn^{4+} = 1, 3, and 5 wt%). 2.0 ml of H_2O_2 mixed with 100 ml of distilled water was used as the complexing agent and the anionic precursor. Beakers (a) and (c) containing respectively the cationic and anionic precursors were heated to 85 °C while those containing distilled water (i.e. beakers b and d) were kept at room temperature. Duration for immersion in cationic and anionic beakers are 20 s each while the time for rinsing in the beaker containing distilled water was 5 s. In this case, a total of 20 cycles was carried out. Varying the number of cycles helps to control the thickness of the deposited films. Similarly, for the deposition of CeO_2, the process was repeated without the addition of Mn^{4+}. The films were annealed at 600 °C for 6 h in order to improve the crystal sizes.

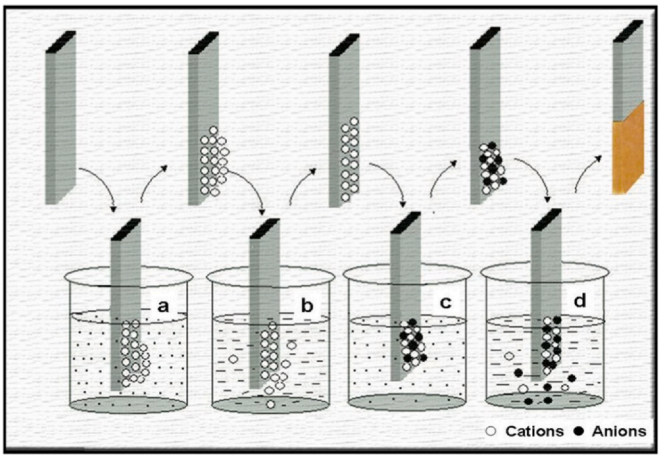

Fig. 1. Schematic representation of SILAR deposition technique.

2.2. Characterization techniques

Atomic force microscope (AFM) operating in tapping mode was used in measuring the topographical structure of the SILAR deposited films. The structure of undoped CeO_2 and Mn-doped CeO_2 were studied on x-ray diffractometer (Rigaku SmartLab diffractometer) with Cu-Kα radiation (λ = 1.540593 Å). XPS measurements were used to determine the binding energies of CeO_2, Mn:CeO_2, Ce 3d, Mn 2p and O 1s from Kratos AXIS Nova Spectrometer (Kratos Analytical Ltd., Canada) using the Al–Kα (1486.74 eV) operating at 250 W (beam power). Optical studies were done via transmittance spectra which was recorded within the wavelength range of 300–1100 nm using Beckman Coulter DU 720 UV-Vis-NIR spectrophotometer with untreated glass as reference. The electrochemical properties of the films were studied using a potentiostat (VersaSTAT MC, Princeton Applied Research) workstation, in a three-electrode set-up. The 0.1 M KOH aqueous solution was used as electrolyte while graphite rod and Ag/AgCl was used as counter electrode and reference electrode respectively.

3. Results and discussion

3.1. X-ray diffraction (XRD) analysis

The x-ray diffraction pattern of CeO_2 and Mn–doped CeO_2 thin films are depicted in Fig. 2. From the patterns, it was evident that ceria based thin films crystallized out in a cubic structure which are indexed to JCPDS No. 34-0394. The Bragg reflections show the fluorite structure of CeO_2 is in strong agreement with those reported in the literature [24–26]. In the Mn-doped samples, there was no indication of additional peaks ascribed to impurities, such as MnO_2. A closer inspection of the most intense peak at 2θ = 28.5° showed slight peak shift towards the lower 2θ angle with a slight increase in the full width at half maximum (FWHM). This indicates the instability and probable structural adjustment in the cubic lattice. Considering the ionic radii of Ce^{4+} (0.97 Å, coordination number, CN = 8) and Mn^{4+} (0.96 Å) as the substituent, the effect of cationic disordering is therefore noted. By using Scherrer, Williamson and Hall equation [27]:

$$\beta_{2\theta} = (k\lambda/D\ \cos\theta) + 4\varepsilon\ \tan\theta \quad (1)$$

(where $\beta_{2\theta}$ = is the line broadening at half the maximum intensity, D = crystalline size, k = shape factor, λ = wavelength of radiation, θ = is

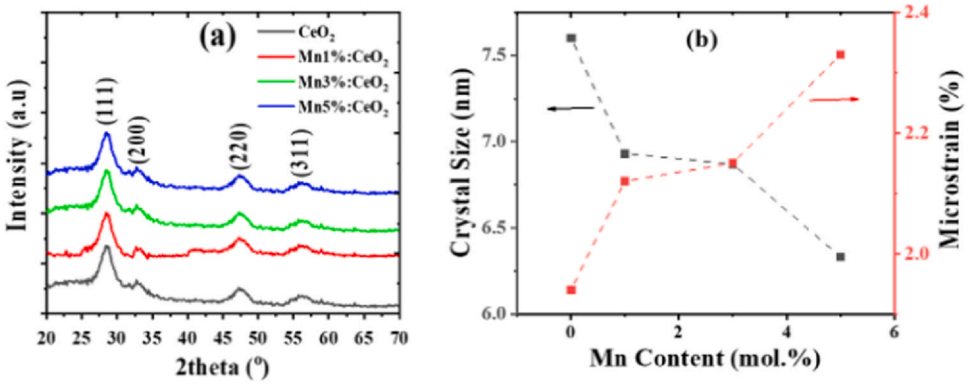

Fig. 2. (a) XRD pattern of as deposited samples of undoped CeO_2 and Mn-doped CeO_2 (b) Variation of the microstrain versus Mn content.

the bragg angle and ε = is the microstain in radians, which is the ratio of peak width to peak position), the crystal size and microstrain of the films were estimated. The obtained results show that crystal size decreases by increased concentration of the dopant whereas the tensile strain increases culminating to ~2.3% for 5 wt% of Mn (see Fig. 2b). This can be explained by slight ionic radii variance between Ce and Mn. However, it is worth noting that the fluorite structure maintained almost its unit cell volume despite the strain.

3.2. X-ray photoelectron spectroscopy (XPS) analysis

XPS was used in quantifying the oxidation states and identifying the differences in the core-line spectra of undoped and Mn-doped CeO_2. Fig. 3a shows the spectrum of CeO_2 and Mn-doped CeO_2 while Fig. 3(b–d) respectively show the XPS spectra of Mn 2p, O 1s and Ce 3d. In the O 1s spectra, the peak at 531.87 eV likely corresponds to the lattice oxygen while the deconvoluted peak at 530.25 eV in the Mn doped CeO_2 may be due to oxygen vacancy in the material arising from mismatch in ionic radii of Ce^{4+} and Mn^{2+}. The peaks at 640.75 eV and 642.23 eV in the Mn 2p XPS spectra (Fig. 3b) demonstrate the presence of Mn^{4+}. In Fig. 3d, the highest binding energy peaks located at 885.02 eV and 881.98 eV are the result of Ce 3d5/2 while the lowest binding energy states are at 881.19 eV and 885.85 eV. Mn 2p peak has significantly split spin-orbit components as well as asymmetric shape for metal. However, the following observations were made: (i) the presence of Ce^{3+} was not noticed and (ii) the dopant (Mn) has no effect on the valence state of Ce.

To show the presence of oxygen in the sample, the O 1s spectrum in figure 3c has its peak at 531.87 eV. This is due to the effect of O^{2-}.

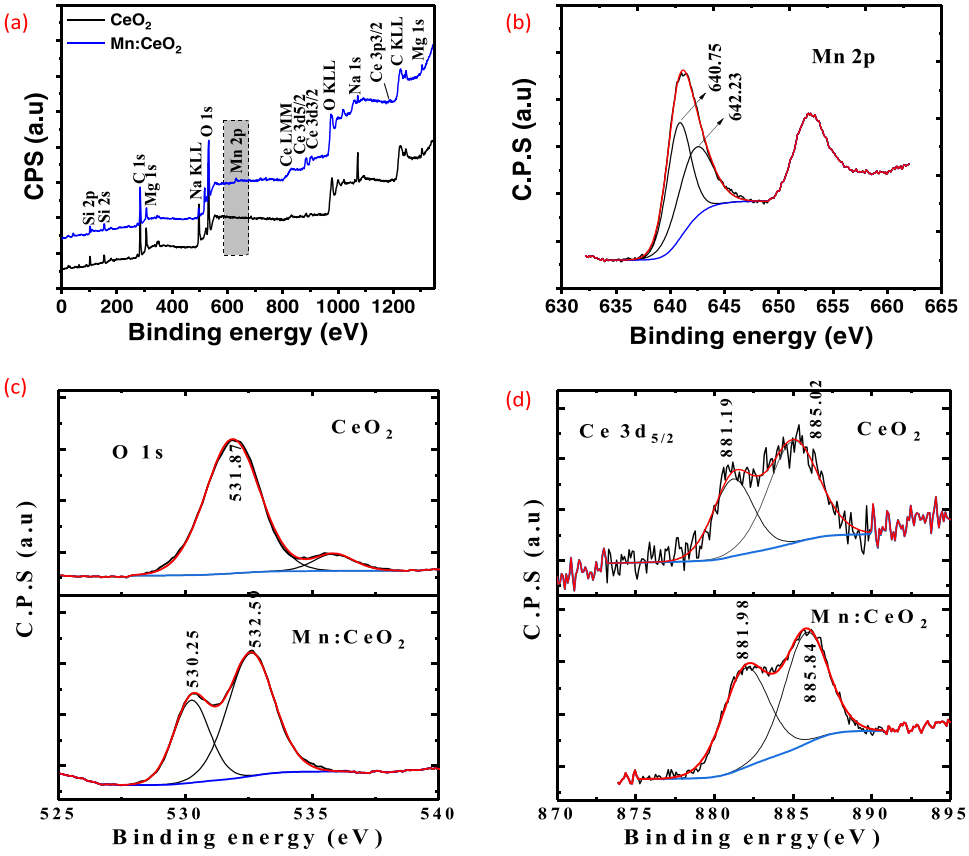

Fig. 3. The XP spectra plots. (a) survey spectra of CeO_2 and Mn-doped CeO_2, (b) Mn 2p spectra, (c) O 1s spectra, (d) Ce 3d spectra.

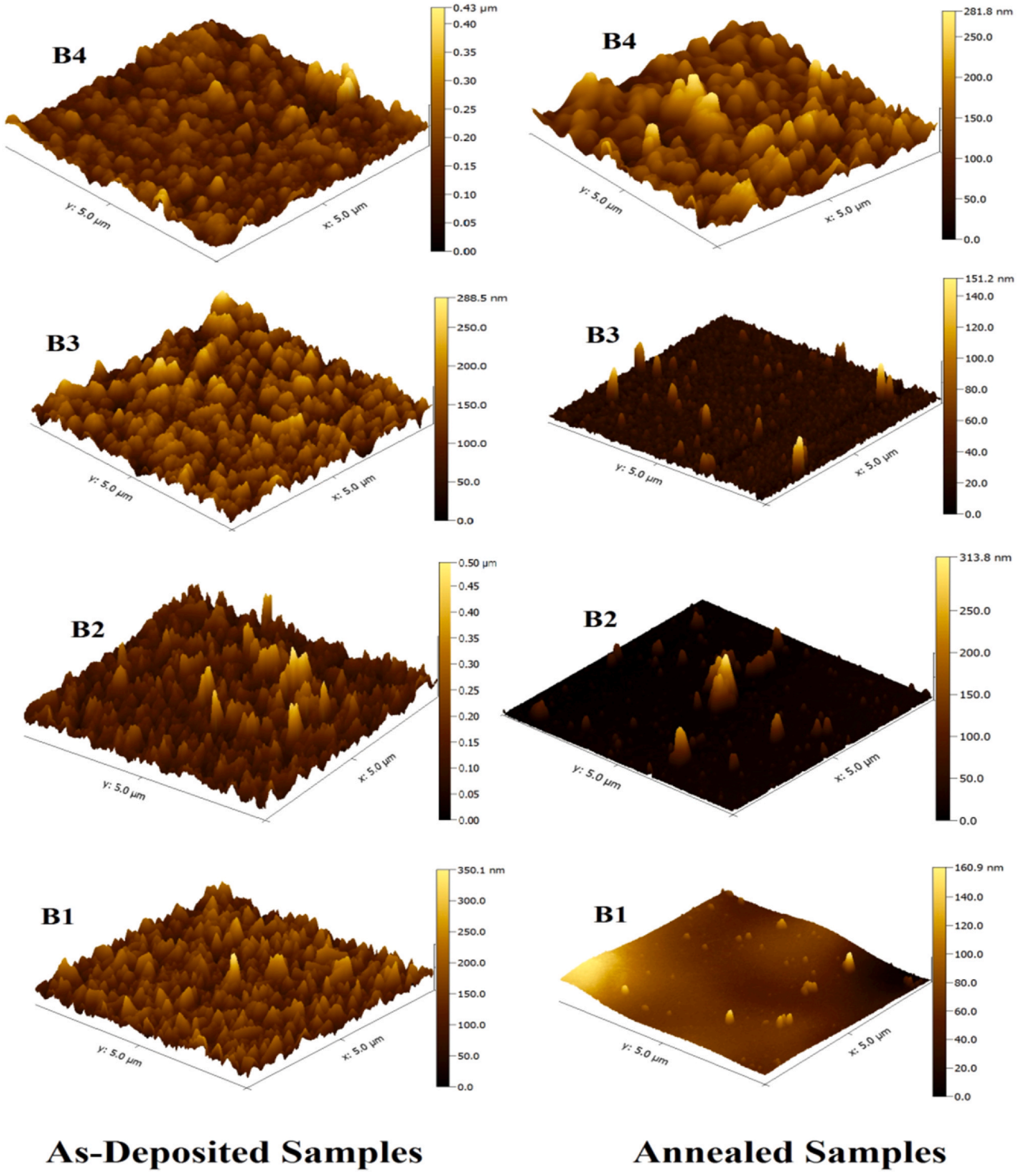

Fig. 4. AFM images showing the roughness of as-deposited and annealed films. (B1, B2, B3 and B4 is the undoped CeO_2, 1 wt%, 3 wt% and 5 wt% Mn-doped CeO_2 respectively).

The interaction of the O—Mn and O—Ce bonds could be attributed to the presence of Mn:CeO_2 which was detected at 532.59 eV in the O 1s peak from the lattice oxygen. This is in agreement with the report of Eric et al. [28].

3.3. Atomic force microscopy (AFM): surface topography and roughness

AFM was used to determine the roughness and surface topography of the deposited films. Fig. 4 displays the AFM images of SILAR deposited undoped and Mn-doped CeO_2 thin films. The undoped and Mn-doped CeO_2 thin films are similar in texture. All the films were crack-free and dense on the surface. Despite the dense nature of the grains, the mean heights are in the range of 200–250 nm for the unannealed films. All the annealed samples appear smoother and more homogenous compared to unannealed samples. Surface roughness analysis as presented in Table 1, show a small increase in roughness as Mn content increases in the annealed films, while no trend was noted in the as-deposited films. Hence, the root mean square value of roughness are 51.8 nm and 26.0 nm respectively for annealed and unannealed 5 wt% Mn-doped CeO_2. The

Table 1
Roughness of undoped and Mn-doped CeO_2 films. (The presented values are Rq values in nm, of 2 μm × 2 μm square areas).

Sample	CeO_2 – Undoped	CeO_2 – 1 wt% Mn-doped	CeO_2 – 3 wt% Mn-doped	CeO_2 – 5 wt% Mn-doped
Roughness (nm) – As-deposited	34.7	44.9	38.4	41.8
Roughness (nm) - Annealed	3.45	6.11	6.46	26.0

Table 2
Grain size of the undoped and Mn-doped CeO_2 films. (Values are the diameter of a circle of equivalent area).

Sample label	CeO_2 – Undoped	CeO_2 – 1 wt% Mn-doped	CeO_2 – 3 wt% Mn-doped	CeO_2 – 5 wt% Mn-doped
Grain size (nm) - As deposited	114.52	48.14	67.42	61.08
Grain size (nm) - Annealed	60.87	28.10	48.93	63.03

5 wt% Mn-doped film was considerably rougher than the lower content films. In the same vein, grain size analysis as shown in Table 2 presents the estimation of the grain sizes of the synthesized thin films.

In general, the grain size estimation suggests smaller grains upon annealing of the films, with the exception of the 5% Mn-doped film. The non-linearity in the grain size after annealing especially at 5% dopant concentration could be attributed to the inability of the dopant to form a ternary compound of high unit cell size with the host lattice at this concentration. The annealed and doped CeO_2 films showed an increase in the grain size as doping concentration increased from 1% to 5%. The reduction in the grain size with annealing could be attributed to the crystallization of the films, which lead to reduction in defects and increase in perfection with concomitant reduction in the grain size. On the other hand, the increase in the grain size of the annealed and Mn doped films suggests that the incorporation of Mn ion enhances the growth of the CeO_2 film.

3.4. Optical absorption studies

Fig. 5 shows that the absorption edge of the nanostructured CeO_2 shifted into the visible region due to the charge transfer transition of ions from 2p (O^{2-}) to 4f (Ce^{4+}) orbitals [29,30]. Hence, the spectral profiles show that the $4f^1 - 5d^1$ transition of Ce^{3+} project with charge transfer transition of Ce^{4+} [31]. The optical band gap (E_g) was evaluated from Eq. (2):

$$E_g = 1240/\lambda \quad (2)$$

where λ is the absorption edge wavelength. From Table 3, the value of E_g for undoped CeO_2 is in agreement with the reports in the literature [30–32]. Comparatively, many authors have also reported this similar trend of the band gap for Mn- and Ni-doped CeO_2 [33,34]. The extensive structural changes observed and reduction in the band gap of CeO_2 as Mn percentage increases could be ascribed to the incorporation of interstitial dopant [34]. The decrease in E_g of annealed 3 wt% and 5 wt% samples can be as a result of the improvement in morphology and crystallinity of the samples.The fusion of Mn ions could be assigned to the presence of the observed peak shift which must be due to oxygen vacancies or impurities [33].

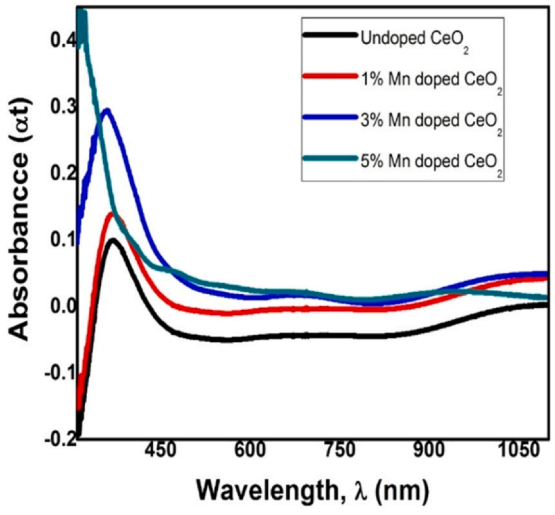

Fig. 5. Optical absorption spectra of the nanostructured undoped and Mn doped CeO_2 thin films.

Table 3
The energy band gap of undoped and Mn-doped CeO_2 of various concentrations.

	Undoped CeO_2	Mn-doped CeO_2 (wt%)		
		1	3	5
Unannealed (eV)	2.38	2.75	3.00	3.19
Annealed (eV)	2.50	2.90	2.85	2.55

Consequently, presence of oxygen vacancies and impurities affects the band gap and also occurred in the formation of transition states. However, narrowing of band gap exhibited by Mn-doped CeO_2 has potential applications in photocatalytic or photovoltaic systems [35].

3.5. Electrochemical studies

3.5.1. Cyclic voltammetry (CV)

Fig. 6 shows the CV curves of undoped and Mn-doped CeO_2 analyzed at different scan rates. The presence of strong redox peaks at each curve is clear evidence that capacitance characteristics are in coordinate with Faradaic reactions. The peaks are due to $Ce^{3+} \leftrightarrow Ce^{4+}$ redox processes. Some responses of CeO_2 and Mn-doped CeO_2 that show pseudocapacitive behavior are:

(i) the presence of noticeable peaks especially at lower scan rates,
(ii) the variation in wt%, produces different shapes of CV curves for different samples and
(iii) the increase in scan rate resulted in the shifts in positive and negative directions of the potential of the cathodic and anodic peaks respectively.

The specific capacitance of CeO_2 and Mn-doped CeO_2 samples can be estimated by using Eq. (3):

$$C_s = \frac{\int Idt}{m\frac{dV}{dt}} \quad (3)$$

where m = the mass of deposit, (dV/dt) = the scan rate, $\int Idt$ = the area under the CV curve and C_s = the specific capacitance (F/g) [36–39]. The specific capacitance values at potential scan rates of 10, 20 and 100 mV/s were observed to be ~410–275 F/g for undoped CeO_2 while for the 1, 3 and 5 wt% Mn films, the values are 486–280 F/g, 509–297 F/g and 690–382 F/g, respectively. At higher scan rate, the specific capacitance value decreases because the ions do not have

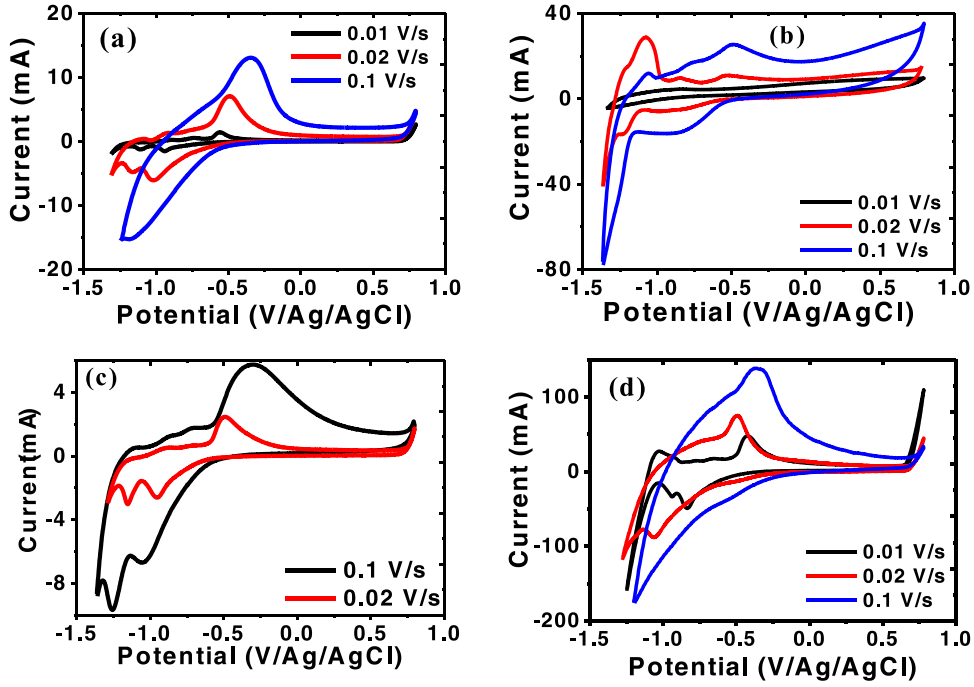

Fig. 6. CV curves at different scan rates of (a) Undoped CeO_2 (b) 1 wt% Mn-doped CeO_2 (c) 3 wt% Mn-doped CeO_2 (d) 5 wt% Mn-doped CeO_2.

Table 4
Specific capacitances from some CeO_2 composites at different synthesis techniques and scan rates.

Electrode	Synthesis Techniques	Specific Capacitance (Fg^{-1})	Scan rate (mVs^{-1})	Ref.
CeO_2/Graphene	Solid State Route	652	5	[11]
CeO_2/Graphene	Solid State Route	110	10	[12]
CeO_2/rGO	Oil bath Method	243	20	[13]
rGO-CeO_2	Hydrothermal Method	91	3	[16]
Mn-doped CeO_2	SILAR	690	10	**This work**

enough time to diffuse through the inner active sites of the electrode while at lower scan rates an increase in specific capacitance was observed due to larger lengths of time permitting better diffusion and intercalation of the ions within the active and interlayer sites. This is in agreement with the report of Nagamuthu et al. [40] and others as shown in Table 4. Most of the Mn doped CeO_2 seen in the literature are not used for supercapacitive application. As evidenced from Table 4, the value we obtained is higher than what previous authors obtained using graphene or reduced graphene oxide to form a composite with CeO_2.

Fig. 7 is the plot of specific capacitance at different scan rate. It can be seen that the increase in scan rate causes a drastic decrease in specific capacitance.Mn-doped CeO_2 films have shown higher specific capacitance than undoped film, this could be as result of its large surface area and porous structure.This is fairly in agreement with the reports of Maheswari et al. [41].

3.5.2. Galvanostatic charge-discharge (GCD)

Fig. 8 shows the galvanostatic charge-discharge curves of undoped and Mn-doped CeO_2 samples plotted as a potential-time graph at different current densities in 0.1 M aqueous KOH electrolytes. From the discharge curve as shown in Fig. 8, we observed the following: (i) a linear variation of potential-time plot which is due to charge separation at the electrode-electrolyte interface; and (ii) a deviation in slope which is a result of the redox reaction between electrolyte and electrodes.

At different applied current densities, the specific capacitance could be derived from the voltage-time measurements plot using Eq. (4):

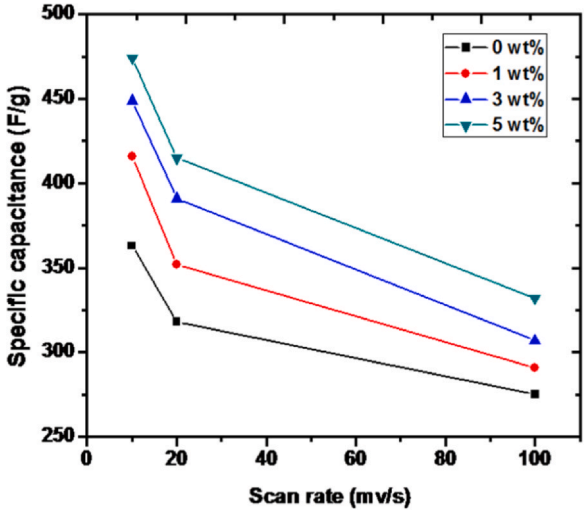

Fig. 7. The specific capacitance of CeO_2 and Mn-doped CeO_2 films at different scan rates for various Mn wt%.

$$C_s = \frac{I\Delta t}{m\Delta V} \tag{4}$$

where $\triangle$v (v) = the potential, $m(g)$ = the mass of the deposit and I (A) = the discharge current for the applied time duration $\triangle t$ (s). From Fig. 8, the evaluated values of specific capacitances for CeO_2 and Mn-doped CeO_2 films at various Mn wt% (0, 1, 3 and 5 wt%) and different current densities of 2, 3 and 4 mA cm^{-2}, were found to be

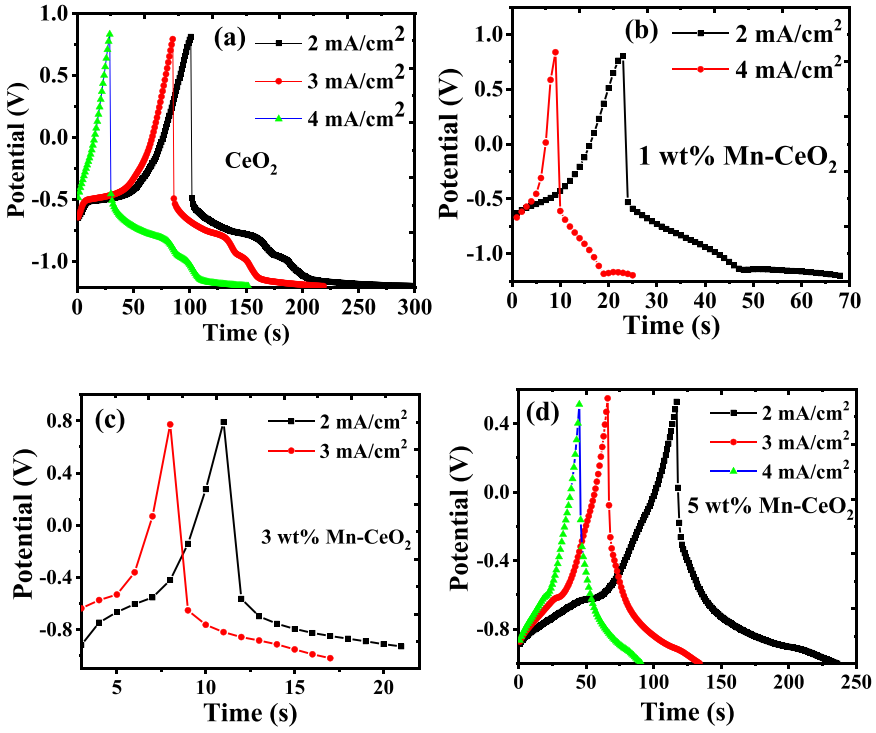

Fig. 8. GCD curves at various scan rates of (a) undoped CeO_2 (b) 1 wt% Mn-doped CeO_2 (c) 3 wt% Mn-doped CeO_2(d) 5 wt% Mn-doped CeO_2.

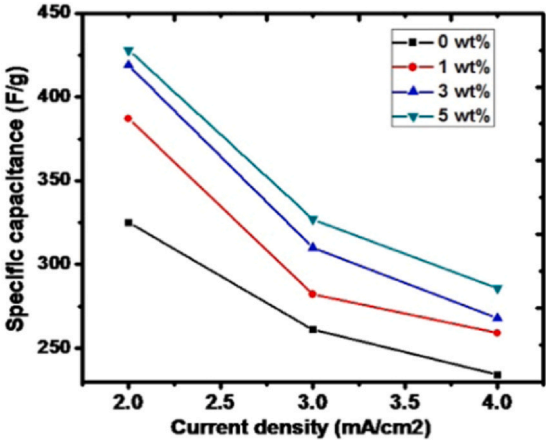

Fig. 9. The specific capacitance against current density of undoped and Mn-doped CeO_2 thin films for various Mn wt% (1, 3 and 5 respectively).

325–234, 387–259, 419–268 and 428–286 Fg^{-1} for 0, 1, 3 & 5 wt% respectively. The specific capacitance value of undoped CeO_2 is quite similar with the report of Maheswari et al. [41]. Due to the increase in surface area, the specific capacitance increases with the increase in the dopant concentration. However, increase in the current density causes lower specific capacitance value in GCD measurements (Fig. 9). Irrespective of how well a device is, the ohmic effect on the polarization due to higher current densities must not be neglected. This is strongly in agreement with the report of Chen et al. [42] and Vijayakumar et al. [43].

3.5.3. Electrochemical impedance spectroscopy

The impedance characteristics of undoped and Mn-doped CeO_2 electrode were evaluated with electrochemical impedance measurement within the frequency range of 100 KHz–100 mHz at potential amplitude of +2.0 V. The Nyquist plots of undoped and Mn-doped CeO_2 have a semicircular arc at the high frequency region which demonstrates the better capacitive performance of the electrodes as shown in Fig. 10. Insets of Fig. 10 shows the equivalent circuit used to model the electrochemical behaviour of CeO_2 electrode and Mn-doped CeO_2.

The characteristic equivalent electrical circuits have the basic components such as charge-transfer resistance (R_{ct}), ohmic resistance (R_s), Warburg resistance (W) and capacitor (C) [44]. The charge transfer resistance depicts the resistance involving the electrokinetics exchange between tetravalent cerium and divalent manganese ions i.e. $Ce^{4+} + Mn^{2+} \rightleftharpoons Mn^{4+} + Ce^{2+}$ as well as the resistance to charge movement at the electrode-electrolyte interface. The Warburg resistance in this case corresponds to the diffusion of ionic species in the bulk electrolytic solution whereas the impedance of the bulk KOH solution is regarded as the ohmic resistance. As observed from Fig. 10, in particular undoped, 1 and 5 wt% Mn doped CeO_2, the Nyquist plot shows a near diagonal at mid to low frequency region, indicating the presence of the Warburg resistance. The diffusion of these ionic species is however known to be slow at high frequency as they do not travel far, thus reducing the Warburg resistance. At low frequency, the diffusion is faster and they travel far; this positively influences the Warburg resistance. For the representative samples, the Warburg resistance is observed to increase/decrease at low/high frequency, again confirming the feature pointed out previously.

The values of charge transfer resistance derived from the experimental results using the equivalent circuit model of undoped and Mn-doped CeO_2 were observed to be 6.87, 9.21, 12.96 and 18.95 Ω for undoped and 1 wt%, 3 wt% and 5 wt% for Mn-doped CeO_2 respectively. It shows that the charge transfer resistance increases with doping, however other structural factors such as the surface area, porosity, lattice defects which improved in the doped samples enhanced the overall specific capacitance obtained from the doped CeO_2.

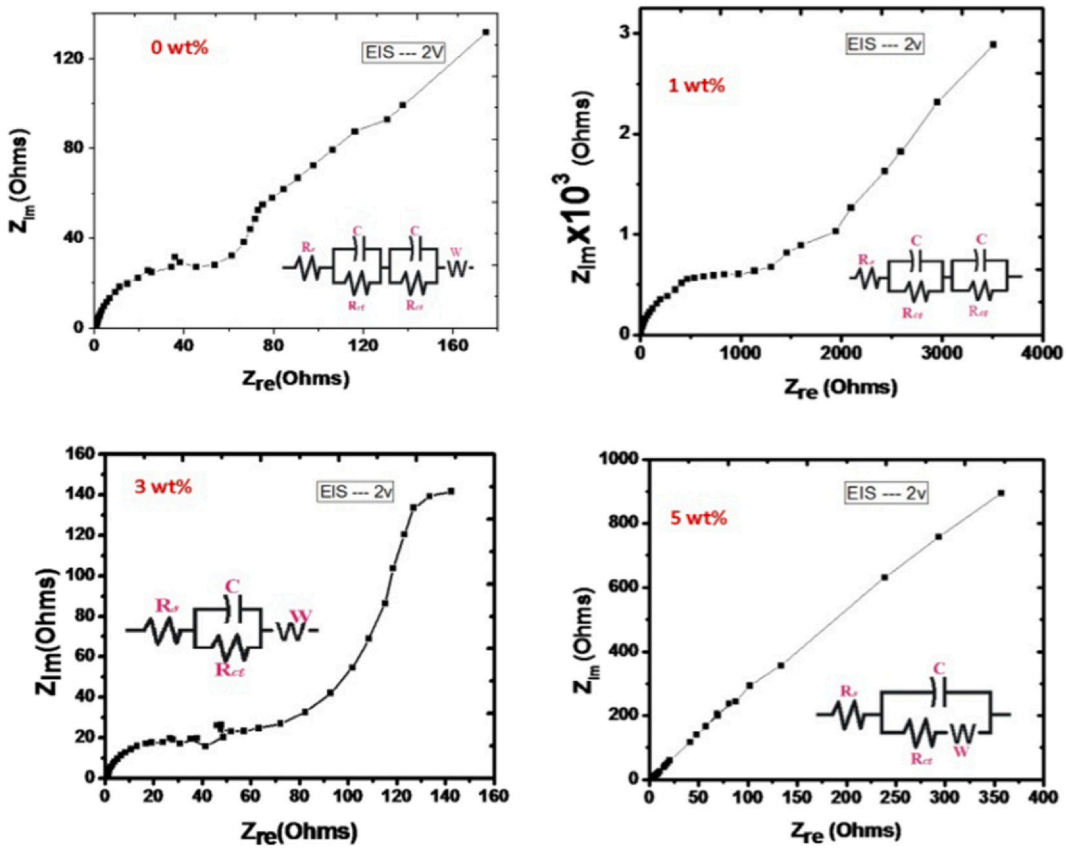

Fig. 10. Nyquist plots of undoped and Mn-doped CeO_2 films for various MnO_2 wt% (1 wt% Mn-doped, 3 wt% Mn-doped and 5 wt% Mn-doped) and the equivalent circuits models.

4. Conclusion

In summary, undoped and Mn-doped CeO_2 thin films electrode materials were successfully synthesized via SILAR method. XRD results confirmed the presence of tensile strain in the fluorite structure of undoped CeO_2 because of its slight difference in the metal radii. The electronic transition was due to impurity transition states within the energy gap culminating to a red shift in the absorption edge of the lattice. The XPS spectrum proves that the manganese oxide exists as Mn^{4+} while the presence of Ce^{3+} was not noticed. AFM topographies revealed a porous network of spherically shaped grains that provided active sites for electrochemical redox reaction. This remarkable property alongside others paved way for high specific capacitance of 690 Fg^{-1} for 5 wt% Mn-doped CeO_2 as proved by cyclic voltammetry.

CRediT authorship contribution statement

Nwachukwu, Iheke Micheal: carried out the laboratory synthsis experiments, Drafted the manuscript. **Assumpta Chinwe Nwanya:** designed the experiments, carried out the electrochemical test and analysis, reviewed and corrected the manuscript. **Rose Osuji:** carried out part of the data analysis and also reviewed the manuscript. **Fabian I. Ezema:** was involved in the experimental design, data analysis as well the manuscript review.

Declaration of Competing Interest

The authors declare that they have no known competing financial interests or personal relationships that could have appeared to influence the work reported in this paper.

Acknowledgements

We thank the Royal Society and the African Academy of Science for the award of Future Leaders African Independent Research (FLAIR) fellowship (FLR\R1\201225) to Dr. A.C. Nwanya. The FLAIR Fellowship Programme is a partnership between the African Academy of Sciences and the Royal Society funded by the United Kingdom (UK) Government's Global Challenges Research Fund.

References

[1] F. Zhao, Y. Wang, X. Xu, Y. Liu, R. Song, G. Lu, Y. Li, Cobalt hexacyanoferrate nanoparticles as a high-rate and ultra-stable supercapacitor electrode material, ACS Appl. Mater. Interfaces 6 (2014) 11007–11012.
[2] G.P. Wang, L. Zhang, J.J. Zhang, A review of electrode materials for electrochemical supercapacitors, Chem. Soc. Rev. 41 (2012) 797–828.
[3] K. Wang, J. Huang, Z. Wei, J. Phys. Chem. C 114 (2010) 8062–8067.
[4] P. Simon, Y. Gogotsi, Materials for electrochemical capacitors, Nat. Mater. 7 (2008) 845–854.
[5] T. Xue, C.L. Xu, D.D. Zhao, X.H. Li, H.L. Li, Electrodeposition of mesoporous manganese dioxide supercapacitor electrodes through self-assembled triblock copolymer templates, J. Power Sources 164 (2007) 953–958.
[6] J.P. Zheng, P.J. Cygan, T.R. Jow, Hydrous ruthenium oxide as an electrode material for electrochemical capacitors, J. Electrochem. Soc. 142 (1995) 2699–2703.
[7] H. Jiang, T. Zhao, J. Ma, C. Yan, C.Z. Li, Ultrafine manganese dioxide nanowire network for high-performance supercapacitors, Chem. Commun. 47 (2011) 1264–1266.
[8] M. Liu, J. Chang, J. Sun, L. Gao, A facile preparation of NiO/Ni composites as high-performance pseudocapacitor materials, RSC Adv. 3 (2013) 8003–8008.
[9] X.H. Xia, J.P. Tu, Y.J. Mai, X.L. Wang, C.D. Gu, X.B. Zhao, Self-supported hydrothermal synthesized hollow Co_3O_4 nanowire arrays with high supercapacitor capacitance, J. Mater. Chem. 21 (2011) 9319–9325.
[10] R.S. Kalubarme, Y.H. Kim, C.J. Park, One step hydrothermal synthesis of a carbon nanotube/cerium oxide nanocomposite and its electrochemical properties, Nanotechnology 24 (2013) 365401–365408.
[11] Y. Wang, C. Xian Guo, J. Liu, T. Chen, H. Yang, Li.C. Ming, CeO_2 nanoparticles/graphene nanocomposite-based high performance supercapacitor, Dalton Trans. 40 (2011) 6388–6391.

[12] T. Saravanan, M. Shanmugam, P. Anandan, M. Azhagurajan, K. Pazhanivel, M. Arivanandhan, Y. Hayakawa, R. Jayavel, Facile synthesis of graphene-CeO_2 nanocomposites with enhanced electrochemical properties for supercapacitors, Dalton Trans. 44 (2015) 9901–9908.
[13] T. Li, H. Liu, A simple synthesis method of nanocrystals CeO_2 modified rGO composites as electrode materials for supercapacitors with long time cycling stability, Powder Technol. 327 (2018) 275–281.
[14] J. Mazloom, F.E. Ghodsi, F.Z. Tepehan, G.G. Tepehan, I. Turhan, Enhanced lithium electrochemical performance and optical properties of CeO_2–SnO_2 nanocomposite thin films by transition metal (TM: Ni, Mn, and Co) doping, J. Sol-Gel Sci. Technol. 86 (2018) 51–62.
[15] B. Ramulu, G. Nagaraju, S.C. Sekhar, J.S. Yu, Highly porous CNTs knotted cerium oxide hollow tubes with exalted energy storage performance for hybrid supercapacitors, J. Alloy. Compd. 819 (2020) 152942.
[16] S. Britto, V. Ramasamy, P. Murugesan, B. Neppolian, T. Kavinkumar, Graphene based ceria nanocomposite synthesized by hydrothermal method for enhanced supercapacitor performance, Diam. Relat. Mater. 105 (2020) 107808.
[17] G. Hua, L. Zhang, G. Fei, M. Fang, Enhanced catalytic activity induced by defects in mesoporous ceria nanotubes, J. Mater. Chem. 22 (2012) 6851–6855.
[18] L. Cui, J. Cui, H. Zheng, Y. Wang, Y. Qin, X. Shu, J. Liu, Y. Zhang, Y. Wu, J.Power Sources 361 (2017) 310–317.
[19] N. Maheswari, G. Muralidharan, Hexagonal CeO_2 nanostructures: an efficient electrode material for supercapacitors, Dalton Trans. 45 (2016) 14352–14362.
[20] Y. Lü, G. Shao, B. Zhao, L. Zhang, J. Wuhan Univ. Technol. Mater. Sci. Ed. 26 (2011) 33–37.
[21] N. Padmanathan, S. Selladurai, Shape controlled synthesis of CeO_2 nanostructures for high performance supercapacitor electrodes, RSC Adv. 4 (2014) 6527–6534.
[22] Lee C.E., Choi S.H., Kim H.Y., Lee S.S., Kim SK., An K.-S. , Ceramics International, 2021, In Press, Corrected Proof.
[23] J. Puišo, S. Tamulevicius, G. Laukaitis, S. Lindroos, M. Leskelä, V. Snitka, Thin Solid Films 457 (2002) 403–404.
[24] F. Abbas, T. Jan, J. Iqbal, I. Ahmad, M.S.H. Naqvi, M. Malik, Facile synthesis of ferromagnetic Ni doped CeO_2 nanoparticles with enhanced anticancer activity, Appl. Surf. Sci. 357 (2015) 931–936.
[25] F.A. Al-Agel, E. Al-Arfaj, A.A. Al-Ghamdi, Y. Losovyj, L.M. Bronstein, W.E. Mahmoud, A novel recipe to improve the magnetic properties of Mn doped CeO_2 as a room temperature ferromagnetic diluted metal oxide, J. Magn. Magn. Mater. 360 (2014) 73–79.
[26] J.M.A. Almeida, P.E.C. Santos, L.P. Cardoso, C.T. Meneses, A simple method to obtain Fe-doped CeO_2 nanocrystals at room temperature, J. Magn. Magn. Mater. 327 (2013) 185–188.
[27] G.K. Williamson, W.H. Hall, X-ray line broadening from filed aluminium and wolfram, Acta Metall. 1 (1953) 22–31.
[28] E. Eric, C. Patrice, P. Danielle, A. St´ephane, F. Gilles, Ce 3d XPS investigation of cerium oxides and mixed cerium oxide (CexTiyOz), Surf. Interface Anal. 40 (2008) 264–267.
[29] Z. Wang, Z. Quan, J. Lin, Remarkable changes in the optical properties of CeO(2) nanocrystals induced by lanthanide ions doping, Inorg. Chem. 46 (13) (2007) 5237–5242.
[30] T. Masui, K. Fujiwara, K. Machida, G. Adachi, T. Sakata, H. Mori, Characterization of cerium(IV) oxide ultrafine particles prepared using reversed micelles, Chem. Mater. 9 (10) (1997) 2197–2204.
[31] L. Yin, Y. Wang, G. Pang, Y. Koltypin, A. Gedanken, Sonochemical synthesis of cerium oxide nanoparticles-effect of additives and quantum size effect, J. Colloid Interface Sci. 246 (1) (2002) 78–84.
[32] S. Maensiri, C. Masingboon, P. Laokul, W. Jareonboon, V. Promarak, P.L. Anderson, S. Seraphin, Egg white synthesis and photoluminescence of platelike clusters of CeO_2 nanoparticles, Cryst. Growth Des. 7 (5) (2007) 950–955.
[33] C.H. Xia, C.G. Hu, P. Chen, B.Y. Wan, X.S. He, Y.H. Tian, Magnetic properties and photoabsorption of the Mn-doped CeO_2 nanorods, Mater. Res. Bull. 45 (2010) 794–798.
[34] A. Thurber, K.M. Reddy, V. Shutthanandan, M.H. Engelhard, C. Wang, J. Hays, et al., Phys. Rev. B 76 (2007) 165206–165213.
[35] A. Corma, P. Atienzar, H. Garc, J.Y. Chane-Ching, Hierarchically mesostructured doped CeO_2 with potential for solar-cell use, Nat. Mater. 3 (2004) 394–397.
[36] D.P. Dubal, G.S. Gund, R. Holze, H.S. Jadhav, C.D. Lokhande, C. Park, Surfactant-assisted morphological tuning of hierarchical CuO thin films for electrochemical supercapacitors, Dalton Trans. 42 (2013) 6459–6467.
[37] A.C. Nwanya, C. Awada, D. Obi, K. Raju, K.I. Ozoemena, R.U. Osuji, A. Ruediger, M. Maaza, F. Rosei, F.I. Ezema, Nanoporous copper-cobalt mixed oxide nanorod bundles as high performance pseudocapacitive electrodes, J. Electroanal. Chem. 787 (2017) 24–35.
[38] A.C. Nwanya, D. Obi, R.U. Osuji, R. Bucher, M. Maaza, F.I. Ezema, Simple chemical route for nanorod-like cobalt oxide films for electrochemical energy storage applications, J. Solid State Electrochem. 21 (2017) (2017) 2567–2576.
[39] I.C. Amaechi, A.C. Nwanya, D. Obi, C. Sebastine, S.C. Ezugwu, A.E. Udounwa, A.B.C. Ekwealor, R.U. Osuji, M. Maaza, F.I. Ezema, Structural characterization and electrochemical properties of cerium–vanadium (Ce–V) mixed oxide films synthesized by chemical route, Ceram. Int. 42 (2016) (2016) 3518–3524.
[40] S. Nagamuthu, S. Vijayakumar, G. Muralidharan, Synthesis of Mn_3O_4/amorphous carbon nanoparticles as electrode material for high performance supercapacitor applications, Energy Fuels 27 (2013) 3508–3515.
[41] N. Maheswari, G. Muralidharan, Int. J. ChemTech Res. 7 (2015) 1185–1190.
[42] Y.C. Chen, Y.K. Hsu, Y.G. Lin, Y.K. Lin, Y.Y. Horng, L.C. Chen, K.H. Chen, Highly flexible supercapacitors with manganese oxide nanosheet/carbon cloth electrode, Electrochim. Acta 56 (2011) 7124–7130.
[43] S. Vijayakumar, S. Nagamuthu, G. Muralidharan, Porous NiO/C nanocomposites as electrode material for electrochemical supercapacitors, ACS Sustain. Chem. Eng. 1 (2013) 1110–1118.
[44] X. Li, J. Rong, B. Wei, Electrochemical behavior of single-walled carbon nanotube supercapacitors under compressive stress, ACS Nano 4 (2010) 6039–6049.